

An augmented correlation framework for the estimation of tumour translational and rotational motion during external beam radiotherapy treatments using intermittent monoscopic X-ray imaging and an external respiratory signal

Doan Trang Nguyen¹, Jeremy T Booth^{2,3}, Vincent Caillet^{1,2}, Nicholas Hardcastle², Adam Briggs², Carol Haddad², Thomas Eade^{1,2}, Ricky O'Brien¹ and Paul J Keall¹

¹ACRF Image X Institute, The University of Sydney - Central Clinical School, NSW 2006, Australia.

²Northern Sydney Cancer Centre, Royal North Shore Hospital, NSW 2065, Australia.

³School of Physics, The University of Sydney, NSW 2006, Australia.

E-mail: d.nguyen@sydney.edu.au

Abstract.

Increasing evidence shows that intrafraction tumour motion monitoring must include both six degrees of freedom (6DoF): 3D translations and 3D rotations. Existing real-time algorithms for 6DoF target motion estimation require continuous intrafraction fluoroscopic imaging at high frequency, thereby exposing patients to additional high imaging dose. This paper presents the first method capable of 6DoF motion monitoring using intermittent 2D kV imaging and a continuous external respiratory signal.

Method: Our approach is to optimise a state-augmented linear correlation model between an external signal and internal 6DoF motion. In standard treatments, the model can be built using information obtained during pre-treatment CBCT. Real-time 6DoF tumor motion can then be estimated using just the external signal. Intermittent intrafraction kV images are used to update the model parameters, accounting for changes in correlation and baseline shifts.

The method was evaluated *in silico* using data from 6 lung SABR patients, with the internal tumour motion recorded with electromagnetic beacons and the external signal from a bellows belt. Projection images from CBCT (10 Hz) and intermittent kV images were simulated by projecting the 3D Calypso beacon positions onto an imager. IMRT and VMAT treatments were simulated with increasing imaging update intervals: 0.1 s, 1 s, 3 s, 10 s and 30 s.

Results: For all the tested clinical scenarios, translational motion estimates with our method had sub-mm accuracy (mean) and precision (standard deviation) while rotational motion estimates were accurate to $< 1^\circ$ and precise to 2° . Motion estimation errors increased as the imaging update interval increased. With the largest imaging update interval (30 s), the errors were 0.1 ± 0.6 mm, -0.0 ± 0.7 mm and 0.1 ± 0.9 mm for translation in the Left-Right, Superior-Inferior and Anterior-Posterior directions, respectively, and $0.1 \pm 1.3^\circ$, $-0.3 \pm 2.0^\circ$ and $0.1 \pm 0.9^\circ$ for rotation around the aforementioned axes for both VMAT and IMRT treatments.

Conclusion: We developed and evaluated a novel method for highly accurate real-time 6DoF motion monitoring on a standard linear accelerator without requiring continuous kV imaging. The proposed method achieved sub-mm and sub-degree accuracy on a lung cancer patient dataset.

1. Introduction

In current radiation therapy, image guided radiation therapy (IGRT) is routinely applied at the start of treatment to align the target with its planned position. However, tumours in the thorax, abdomen and pelvis are not static during treatment. Hence, methods to monitor tumour motion during treatment are highly desirable, even more so with dose escalation and hypofractionation.

A number of different methods have been developed and clinically tested for real-time intrafraction motion monitoring. Systems such as CyberKnife (Accuray, Sunnyvale, CA) (Hoogeman et al. 2009), ExacTrac (BrainLab, Munich, Germany) (Stevens et al. 2016) and the real-time tracking radiotherapy (RTRT) system use real-time kilovoltage (kV) images from two (CyberKnife and ExacTrac) or four (RTRT system) orthogonal room-mounted imagers to track the tumour position based on segmented positions of implanted fiducial markers (Kitamura et al. 2002, Sazawa et al. 2009, Shirato et al. 2003). Commercial solutions including Calypso (Varian, Palo Alto, CA) (Kupelian et al. 2007) and RayPilot (Micropos, Gothenburg, Sweden) (Castellanos et al. 2012) utilise implanted electromagnetic transponders and transmitters, respectively, transmitting positional signals to an external receiver. Emerging real-time guidance technologies include ultrasonography (Ballhausen et al. 2015) and integrated magnetic resonance imaging (MRI)-radiation therapy systems (Fallone et al. 2009, Raaymakers et al. 2009). Common to all these methods is the need for additional dedicated and typically expensive equipment to perform the real-time guidance.

Ideally, real-time image guidance would be performed using a standard linear accelerator (linac) without relying on additional hardware. To this end, a number of algorithms have been proposed for the purpose of estimating the target's position in 3D based on its location on a 2D image, which can be acquired using a linear accelerator gantry mounted kilovoltage (kV) X-ray imager system (Poulsen et al. 2008, Li et al. 2011, Chung et al. 2016, Shieh et al. 2017).

An apparent advantage of utilising the kV imager is that: most modern linacs have a kV imager, mounted orthogonally to the treatment beam. However, as the target position on the kV imager only contains 2D information, a 2D–3D target position conversion is often required. One significant drawback to using kV imaging during treatment is the additional radiation dose to the patient due to continuous X-ray imaging. Cho et al. (2010) described a general framework allowing occasional kV imaging during treatment by utilising an external respiratory signal. The source of the external signal can come from either optical surface monitoring devices such as RPM (Varian, Palo Alto, CA), Optical Surface Monitoring System (OSMS) (Varian, Palo Alto, CA), AlignRT (VisionRT, London, UK), Catalyst (C-RAD, Uppsala, Sweden) or volumetric or spirometric measurements such as the bellows belt (Philips Healthcare, Amsterdam, Netherlands). These devices are becoming increasingly common in a modern radiotherapy department. This method allows X-ray images to be taken less often and thereby significantly reduces imaging dose to the patient. Although the

original method has been extended (Cho et al. 2012) to account for phase mismatch between the external signal and internal tumour motion and clinically implemented (Bertholet et al. 2018), one drawback to this body of work is that it only computes 3D target translation and not rotation.

Increasing evidence suggests that intrafractional tumour motion corrections should be applied for both tumour translation and tumour rotation (Rijkhorst et al. 2009, Wu et al. 2011, Amro et al. 2013). Retrospective post-treatment calculations of tumour rotation have shown that the rotations could be significant for both prostate and lung tumours (Amro et al. 2013, Aubry et al. 2003). Dosimetrically, uncorrected prostate rotations of 15° can result in a 12% underdose to the tumour (Rijkhorst et al. 2009). Tumour rotation estimation using Kilovoltage Intrafraction Monitoring (KIM) has been developed using the iterative closest point (ICP) algorithm (Tehrani et al. 2013). This method has been used retrospectively to quantify translational and rotational motion for prostate and lung cancers (Huang et al. 2015) and liver cancer (Bertholet et al. 2016), and prospectively in the TROG 15.01 SPARK trial (Nguyen et al. 2017). A disadvantage of this method is that the rotational motion can only be solved after the translational motion as the ICP algorithm requires target positions in 3D, which usually comes from a 2D–3D estimation framework.

In this work, we propose a novel algorithm to compute tumour 6DoF motion from an external signal and intermittent imaging information. The proposed method utilises the inherent correlations between the external respiratory signal and the internal tumour motion, hence is named the 6D Internal-External Correlation (6D-IEC) framework. This framework uses tumour positions from 2D imaging during routine pre-treatment Cone Beam CT (CBCT) to build the first correlation model, which can then be used to track the tumour 6DoF motion during treatment with the external respiratory signal. Intermittent intrafraction imaging is used to update the correlation model. The framework is designed to work with a kV image segmentation system to extract tumour or radio-opaque markers representing the tumour positions during both CBCT and intrafraction imaging. Thus, the framework is applicable for any linear accelerator systems equipped with a kV imaging system and any of the external respiratory signal without requiring any additional dedicated hardware.

2. Method

In this section, we first describe the formalism of a novel method for estimating 6DoF motion from a one dimensional external respiratory signal and intermittent 2D projections of a target using a least square method. Then, we describe the IMRT and VMAT simulations used to comprehensively evaluate the proposed algorithm, based on the patients' lung data, acquired using the Calypso electromagnetic localisation system (Varian, CA, USA). Throughout this paper, we use the IEC 61217 coordinate system to describe the patient's motion relative to the treatment beam. According to this coordinate system, the motion in the x -direction corresponds to the Left-Right (LR)

direction, the y -direction corresponds to the Superior-Inferior (SI) direction and the z -direction corresponds to the Anterior-Posterior (AP) direction of a patient in the treatment room in the head-first supine orientation.

2.1. 6D-IEC algorithm

2.1.1. Learning phase

The relationship between the external respiratory signal and the internal target motion $s(t)$ can be defined as a composite linear correlation:

$$(\hat{\mathbf{T}}_{\mathbf{r}}; \hat{\boldsymbol{\varphi}})(t) = \begin{pmatrix} \hat{T}_{rx} \\ \hat{T}_{ry} \\ \hat{T}_{rz} \\ \hat{\alpha} \\ \hat{\beta} \\ \hat{\gamma} \end{pmatrix} = \begin{pmatrix} a_x \\ a_y \\ a_z \\ a_\alpha \\ a_\beta \\ a_\gamma \end{pmatrix} \cdot s(t) + \begin{pmatrix} b_x \\ b_y \\ b_z \\ b_\alpha \\ b_\beta \\ b_\gamma \end{pmatrix} \cdot s(t-\lambda) + \begin{pmatrix} c_x \\ c_y \\ c_z \\ c_\alpha \\ c_\beta \\ c_\gamma \end{pmatrix} = \mathbf{a} \cdot s(t) + \mathbf{b} \cdot s(t-\lambda) + \mathbf{c} \quad (1)$$

where $\hat{\mathbf{T}}_{\mathbf{r}} = (\hat{T}_{rx} \hat{T}_{ry} \hat{T}_{rz})^T$ is the translation vector around the $[x, y, z]$ axes of the transformation equation, respectively and the angles $\boldsymbol{\varphi} = (\alpha \beta \gamma)^T$ are the rotations angles around the $[x, y, z]$ axes, respectively. In the Equation(1), the parameter λ is a time-augmented parameter, following the work of Ruan et al. (2008).

Together, the parameters $\hat{\mathbf{T}}_{\mathbf{r}}(t)$ and $\boldsymbol{\varphi}(t)$ can be used to calculate the linear transformation between the original orientation and position \mathbf{M}_{ref} and the current position and orientation $\mathbf{M}(t)$ of the target:

$$\mathbf{M}(t) = \begin{pmatrix} x_1 & x_2 & \cdots & x_n \\ y_1 & y_2 & \cdots & y_n \\ z_1 & z_2 & \cdots & z_n \end{pmatrix} (t) = \begin{pmatrix} \mathbf{x} \\ \mathbf{y} \\ \mathbf{z} \end{pmatrix} (t) = \mathbf{R}(t) \cdot \mathbf{M}_{\text{ref}} + \hat{\mathbf{T}}_{\mathbf{r}}(t) \quad (2)$$

where:

$$\mathbf{R}(t) = \mathbf{R}_x(t) \mathbf{R}_y(t) \mathbf{R}_z(t) = \begin{pmatrix} \cos \beta \cos \gamma & -\cos \beta \sin \gamma & \sin \beta \\ \cos \alpha \sin \gamma + \sin \alpha \sin \beta \cos \gamma & \cos \alpha \cos \gamma - \sin \alpha \sin \beta \sin \gamma & -\sin \alpha \cos \beta \\ \sin \alpha \sin \gamma - \cos \alpha \sin \beta \cos \gamma & \sin \alpha \cos \gamma + \cos \alpha \sin \beta \sin \gamma & \cos \alpha \cos \beta \end{pmatrix} \quad (3)$$

Additionally, if the current orientation and position of the target $\mathbf{M}(t)$ is estimated from Eq.(1) as $\hat{\mathbf{M}}(t)$, then we can estimate the projected positions of $\hat{\mathbf{M}}(t)$ using the projection equation:

$$\hat{\mathbf{P}}(\hat{\mathbf{M}}(t)|\theta) = \begin{pmatrix} \hat{\mathbf{u}} \\ \hat{\mathbf{v}} \end{pmatrix} = \frac{SID}{SAD - (\hat{\mathbf{x}} \cdot \cos \theta + \hat{\mathbf{z}} \cdot \sin(\theta))} \begin{pmatrix} \hat{\mathbf{x}} \cdot \sin(\theta) - \hat{\mathbf{z}} \cdot \cos(\theta) \\ \hat{\mathbf{y}} \end{pmatrix} \quad (4)$$

with:

- $(\hat{\mathbf{u}} \ \hat{\mathbf{v}})^T$: the position of the target on the imager,
- SID: the X-ray Source to Imager Distance of the system,
- SAD: the X-ray Source to Axis (Isocentre) Distance of the system.

Thus, after a learning phase where the actual projected positions $(\mathbf{u} \ \mathbf{v})^T$ are detected, the parameters \mathbf{a} , \mathbf{b} and \mathbf{c} of the correlation equation (Eq.1) can be found by minimising the sum of the distances between the estimated positions $(\hat{\mathbf{u}} \ \hat{\mathbf{v}})^T$ and the actual projected positions over F number of imaging frames:

$$(\mathbf{a}, \mathbf{b}, \mathbf{c}) = \arg \min \left\| \sum_{f=0}^{f=F} \sum_{n=1}^{n=N} |u_f^n - \hat{u}_f^n| + |v_f^n - \hat{v}_f^n| \right\|_2 \quad (5)$$

where N is the number of points or markers representing the target \mathbf{M} . In order to find a unique orientation \mathbf{R} for the target \mathbf{M} , the minimum number of points required is 3.

However, the state augmentation parameter λ in Eq.1 cannot be found with the aforementioned minimisation process. Therefore, we iteratively find λ by choosing the λ parameter that produces the smallest mean estimation error over the learning period using the cost function in Eq.5. The algorithm below shows the actual implementation of the 6D-IEC algorithm at the end of the learning phase. In this implementation, the state augmentation parameter λ is an integer number of frames. For the *in silico* simulation, each frame corresponded to 100 ms.

2.1.2. Tracking phase

During the tracking phase, the correlation parameter is known, thus, the current tumour position could be estimated as soon as the signal $s(t)$ became available. In order to ascertain the model is up to date, an update of the correlation model occasionally is required. This could be done as soon as a new projection image arrived.

2.2. Evaluation with *in-silico* simulations

Figure 1 shows the overall *in silico* simulations for evaluation of the 6D-IEC algorithm using lung cancer patient data.

2.2.1. Ground-truth data

To characterise the performance and retrospectively validate our method, patient data were obtained from the multi-leaf collimator (MLC) tracking Stereotactic Ablative Body Radiotherapy (Light-SABR) clinical trial (NCT02514512) (Booth et al. 2016).

The internal tumour motion was obtained using electromagnetic transponders implanted near the tumours. Additionally, a respiratory bellows belt (Philips Medical System, Cleveland, OH) was wrapped around the patient's abdomen to monitor the external breathing pattern during treatment delivery. The belt was equipped with

Algorithm 1 6D-IEC algorithm at the end of the learning phase. N: the upper limit of λ iteration, set to $N = 2.5$ s for the *in silico* experiments. s.t.: such that. NLLS: non-linear least square optimisation.

```

for  $\lambda_i = 0:N$ 
     $[\sim, \sim, \sim, \sim, E(i)] \leftarrow \text{compute6DIEC}(s_t, (\mathbf{u} \mathbf{v})^T, \mathbf{M}_{\text{ref}}, \lambda_i);$ 
end for
 $\lambda = \lambda_i$  s.t.  $\min(E)$ ;
 $[\mathbf{a}, \mathbf{b}, \mathbf{c}, \text{estimated6DoF}, E] \leftarrow \text{compute6DIEC}(s_t, (\mathbf{u} \mathbf{v})^T, \mathbf{M}_{\text{ref}}, \lambda);$ 

function  $\text{compute6DIEC}(s_t, (\mathbf{u} \mathbf{v})^T, \mathbf{M}_{\text{ref}}, \lambda)$ 
    % Compute the augmented respiratory signal
     $s_{t-\lambda} \leftarrow s_t(t - \lambda);$ 
    %Define Convergence threshold
     $T = 10^{-3};$ 
    % Initialise optimisation seeds
     $[\mathbf{a}_0, \mathbf{b}_0, \mathbf{c}_0] = 0;$ 
    while  $|E - E_{temp}| > T$ 
        % E: sum of squared estimation errors
         $E \leftarrow E_{temp};$ 
        % Optimise to solve for  $[\mathbf{a}, \mathbf{b}, \mathbf{c}]$  (eqs. 1 to 5)
         $[\mathbf{a}, \mathbf{b}, \mathbf{c}, E_{temp}] \leftarrow \text{NLLS}(s_t, s_{t-\lambda}, (\mathbf{u} \mathbf{v})^T, \mathbf{M}_{\text{ref}}, \text{seeds} = [\mathbf{a}_0, \mathbf{b}_0, \mathbf{c}_0]);$ 
        % Randomly move the seeds to reduce the probability of local minima
         $[\mathbf{a}_0, \mathbf{b}_0, \mathbf{c}_0] \leftarrow [\mathbf{a}, \mathbf{b}, \mathbf{c}] + 0.1 * \text{rand}([0 : 1]);$ 
    end while
     $\text{estimated6DoF} \leftarrow \mathbf{a} * s_t + \mathbf{b} * s_{t-\lambda} + \mathbf{c};$ 
    return  $[\mathbf{a}, \mathbf{b}, \mathbf{c}, \text{estimated6DoF}, E];$ 
end function

```

a strain gauge coupled with a sensor to record pressure variation induced by chest stretching during breathing.

Manual synchronisation between bellows belt respiratory signal (40 Hz) and internal tumour motion represented by 3 or more implanted transponders (10 Hz) was performed using events such as a short apnea or a patient cough. Only the average SI positions of the available transponders' positions in each fraction were used to perform synchronisation so that the synchronisation step would not bias the results.

The ground-truth data for this study include the first seven patients of the Light-SABR trial. The data from one patient, who was treated in the lateral recumbent position, were excluded because the amplitude of the respiratory signal was too small. In the remaining 6 patients, 3 patients were treated in the prone position while the other 3 patients were treated in the supine position. Nineteen of the 24 fractions, with both transponders and bellows belt data, were used as the ground-truth dataset.

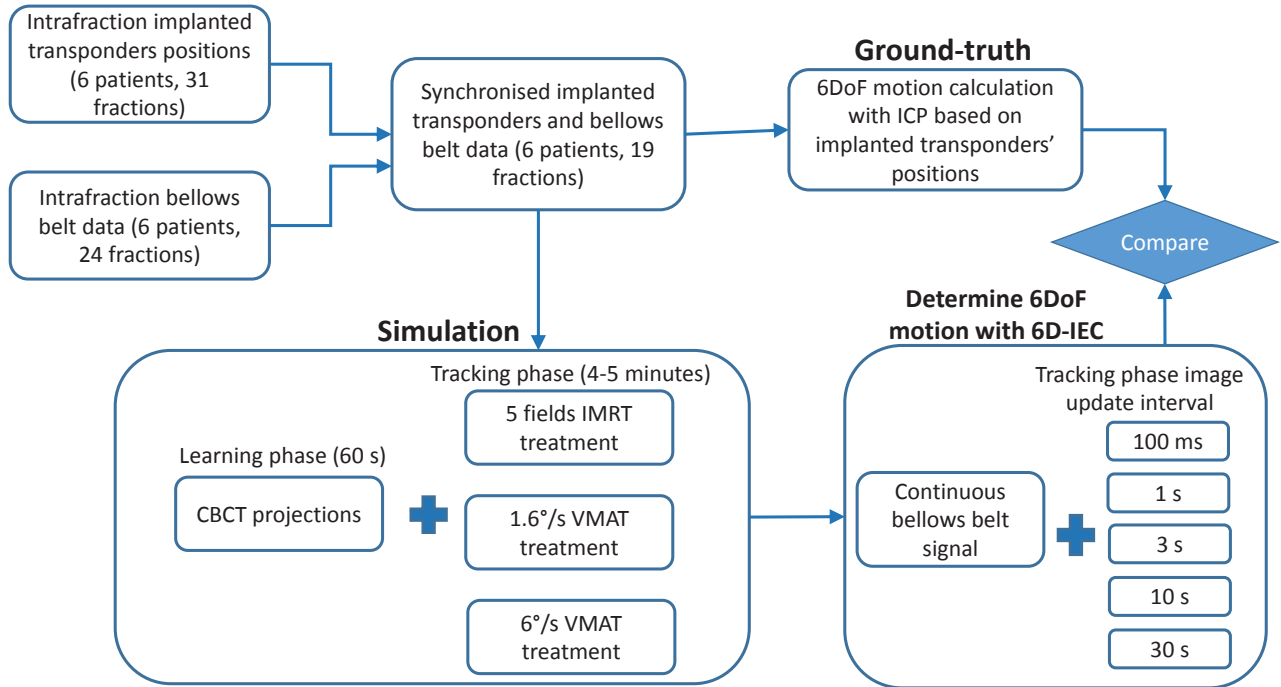


Figure 1. A schematic diagram of the method used to investigate the accuracy and precision of the 6D-IEC algorithm.

Data from the five fractions not included were missing features that could be used to reliably synchronise the internal tumour motion and bellows belt data. Finally, 6DoF intrafraction target motion of each fraction was computed from the 3D positions of the transponders during treatments using the ICP algorithm (Tehrani et al. 2013). The positions and poses of the transponders at the beginning of each fraction were used as the reference positions.

2.2.2. Simulation

In order to test the accuracy of the proposed 6D-IEC algorithm in estimating 6DoF motion, for each patient trajectory in the ground-truth dataset, the ground-truth 3D positions of the transponders were projected onto an imager using equation (4). The SAD and SID value were set at 1000 mm and 1800 mm, respectively. This projection step is to simulate a realistic scenario during treatment in which radio-opaque implanted markers can be segmented from intrafraction kV images.

All simulations started with the gantry rotated from 180° at the speed of $6^\circ/\text{s}$ for the first 60 s (Figure 1). This was to simulate the initial Cone Beam Computed Tomography (CBCT) procedure at the beginning of each fraction. The CBCT period was used as the learning phase for 6D-IEC to build the first correlation model. The imaging rate was simulated at 10 Hz during the CBCT phase.

Three clinical treatment scenarios were tested. In the first scenario, an IMRT

treatment with 5 fields was simulated following the initial 60 s CBCT. For the IMRT treatment, the linac gantry angles (MV) were set at 250° , 310° , 0° , 60° and 110° with the delivery time for each field set at 40 s. In another scenario, the gantry speed was set at $1.6^\circ/\text{s}$ to simulate VMAT lung SABR treatment with flattening filter. In fact, this was the typical gantry speed for VMAT treatment in the aforementioned clinical trial from which came the ground-truth dataset. In the third testing scenario, the gantry speed was set at $6^\circ/\text{s}$ to simulate lung SABR treatment without flattened filter. Excluding the CBCT learning period, each tested trace included between 4 and 5 minutes of intrafraction motion.

During the simulated treatment phase, for each treatment scenario, the 6D-IEC algorithm was evaluated for different imaging update intervals during the tracking period, including: 0.1 s, 1 s, 3 s, 10 s and 30 s.

2.2.3. Evaluation of 6D-IEC estimation

To evaluate the accuracy and precision of 6D-IEC in estimating 6DoF motion, 6D-IEC motion estimation was compared against the ground-truth 6DoF motion, as shown in Figure 1. The difference between 6D-IEC estimation and the ground-truth was reported. Herein, we refer to this difference between 6D-IEC estimates and the ground-truth as *error*.

Furthermore, we evaluated the factors that could affect the accuracy and precision of 6D-IEC using the Pearson correlation test, including:

- Range of motion in each tested patient tumour trajectory: the standard deviation of error in each degree of freedom were evaluated against the standard deviation of motion in the corresponding degree of freedom.
- Motion magnitude: the estimation error at each point was evaluated against the magnitude of motion in each degree of freedom.
- Correlation between external signal and internal motion in each degree of freedom: the standard deviation of error for each trace was evaluated against the correlation between each degree of freedom internal motion and the external bellows signals.
- Deformation: we computed the correlation between the estimation error at each time point and the magnitude of deformation, calculated as the difference between the area of the 3D triangle formed by the 3 beacons at the same time point and at time 0 (referenced positions).
- State augmentation parameter λ : we evaluated the relationship between estimation errors for each tested motion trace and the state augmentation parameter λ found for each motion trace using the aforementioned iterative method.

These tests were applied to the best and worst results of the tested clinical scenarios.

Clinical Scenario	Imaging Interval	LR(mm)	SI(mm)	AP(mm)	rLR($^{\circ}$)	rSI($^{\circ}$)	rAP($^{\circ}$)
IMRT	0.1 s	0.1 \pm 0.6	-0.0 \pm 0.6	0.0 \pm 0.8	0.1 \pm 1.3	-0.2 \pm 1.8	0.1 \pm 0.9
	1 s	0.1 \pm 0.6	-0.0 \pm 0.7	0.0 \pm 0.8	0.2 \pm 1.3	-0.3 \pm 2.0	0.1 \pm 0.9
	3 s	0.1 \pm 0.6	-0.0 \pm 0.7	0.1 \pm 0.9	0.2 \pm 1.3	-0.3 \pm 2.0	0.1 \pm 0.9
	10 s	0.1 \pm 0.6	-0.0 \pm 0.7	0.1 \pm 0.9	0.2 \pm 1.3	-0.3 \pm 2.0	0.1 \pm 0.9
	30 s	0.1 \pm 0.6	-0.0 \pm 0.7	0.1 \pm 0.9	0.2 \pm 1.3	-0.3 \pm 2.0	0.1 \pm 0.9
VMAT 1.6 $^{\circ}$ /s	0.1 s	0.0 \pm 0.6	-0.0 \pm 0.6	0.0 \pm 0.8	0.2 \pm 1.3	-0.3 \pm 1.8	0.1 \pm 0.9
	1 s	0.1 \pm 0.6	-0.0 \pm 0.7	0.1 \pm 0.8	0.2 \pm 1.3	-0.3 \pm 1.9	0.1 \pm 0.9
	3 s	0.1 \pm 0.6	-0.0 \pm 0.7	0.1 \pm 0.9	0.2 \pm 1.3	-0.3 \pm 1.9	0.1 \pm 0.9
	10 s	0.1 \pm 0.6	-0.0 \pm 0.7	0.1 \pm 0.9	0.2 \pm 1.3	-0.3 \pm 2.0	0.1 \pm 0.9
	30 s	0.1 \pm 0.6	-0.0 \pm 0.7	0.1 \pm 0.9	0.2 \pm 1.3	-0.3 \pm 2.0	0.1 \pm 1.0
VMAT 6 $^{\circ}$ /s	0.1 s	0.1 \pm 0.6	-0.0 \pm 0.6	0.0 \pm 0.8	0.1 \pm 1.2	-0.3 \pm 1.8	0.1 \pm 0.9
	1 s	0.1 \pm 0.6	-0.0 \pm 0.7	0.0 \pm 0.8	0.1 \pm 1.3	-0.3 \pm 1.9	0.1 \pm 0.9
	3 s	0.1 \pm 0.6	-0.0 \pm 0.7	0.0 \pm 0.9	0.1 \pm 1.3	-0.3 \pm 1.9	0.1 \pm 0.9
	10 s	0.1 \pm 0.6	-0.0 \pm 0.7	0.0 \pm 0.9	0.1 \pm 1.3	-0.3 \pm 1.9	0.1 \pm 0.9
	30 s	0.1 \pm 0.6	-0.0 \pm 0.7	0.0 \pm 0.9	0.1 \pm 1.3	-0.3 \pm 1.9	0.1 \pm 0.9

Table 1. Mean and standard deviation of error of 6D-IEC in estimating 6DoF internal tumour motion from external signal with intermittent imaging during treatment compared to the ground-truth from implanted electromagnetic transponders.

3. Results

3.1. Accuracy of 6D-IEC

For this section, the translational motion is denoted by its axis of motion, e.g, translational motion in LR is denoted as LR. The rotational motion is denoted by an r before its axis of rotation, e.g rotational motion around the SI axis is denoted as rSI. This is simply for clarity in figures.

Table 1 reports the mean and standard deviation of the difference between 6D-IEC estimated motion and the ground-truth. For all the tested clinical scenarios, across all the tested imaging update intervals, in estimating translational motion, 6D-IEC was both accurate (mean of errors) and precise (standard deviation of errors) to within 1 mm of the ground-truth. In estimating rotational motion, 6D-IEC was accurate to within 1 $^{\circ}$ and precise to within 2 $^{\circ}$ across all the imaging update intervals.

Figure 2 shows the boxplots of the error of 6D-IEC in estimating 6DoF lung tumour motion compared to the ground-truth motion measured with the Calypso electromagnetic system. Overall, in each of the imaging update intervals during the tracking phase, the errors in all 6DoFs were similar for both IMRT and VMAT treatment scenarios (gantry speed of 1.6 $^{\circ}$ /s and 6 $^{\circ}$ /s). As shown in the boxplots, in estimating translational motion, 99.9% of 6D-IEC estimates were within ± 2 mm of the ground-truth for an imaging update interval of 1 s or lower. The largest errors of translational motion estimation with 6D-IEC were in the AP direction. At the largest tested imaging update interval of 30 s, 99.9% errors for AP were between ± 2.5 mm. For the rotational motion

estimation, the largest errors were in the rotations around the SI axis with a 99.9% interval of error of $\pm 4.2^\circ$. In all tested scenarios, the standard deviation of translational and rotational errors increased slightly as the imaging update interval increased. Figure 3 shows the distributions of the geometric errors in all six degrees of freedom for the imaging updating interval of 30 seconds.

Figure 4 shows two cases in which 6D-IEC was successful in estimating the 6DoF motion and Figure 5 shows two examples in which there were large errors in estimating 6DoF motion with 6D-IEC. These cases demonstrated the performance of 6D-IEC in estimating 6DoF motion with different characteristics, magnitude and periods. The results shown in Figures 4 and 5 were 6D-IEC estimated motion in the clinical scenario of slow VMAT gantry rotation ($1.6^\circ/s$) with the largest tested imaging update interval of 30 s during the tracking phase.

3.2. Factors affecting 6D-IEC estimation accuracy

Figures 6 to 10 show the relationships between 6D-IEC errors and the different tested factors that may affect the performance of 6D-IEC in estimating 6DoF motion as scatter plots. Fitted lines are added to the scatter plot of the variable pairs with strong correlations ($\rho > 0.5$ or $\rho < -0.5$). As seen in these figures, the extent to which each of the tested factors correlated with the estimating error by 6D-IEC were similar for both the best tested clinical scenario (VMAT $6^\circ/s$ with 100 ms imaging update interval) and the worst tested clinical scenario (VMAT $1.6^\circ/s$ with 30 s imaging update interval). Wherever there was a strong relationship, the correlation value increased slightly in the worst case.

As shown in Figure 6, there was a strong correlation between the standard deviation of error and the range of motion in each degree of freedom in the tested dataset. All of the value pairs had a Pearson correlation coefficient above 0.8, except for the SI translational motion ($\rho < 0.5$). In terms of the range of motion in the tested dataset, the motion in the SI direction had the largest range for translational motion while the rotation around the SI axis had the largest motion range for rotational motion.

Interestingly, although the estimating error of 6D-IEC increased with the motion range of each trace as evident by the high positive Pearson correlation coefficient (Figure 6), there was no strong correlation between the estimating error magnitude and the magnitude of the motion at each time point, as shown in Figure 7. Additionally, we did not find any strong correlation between the magnitude of deformation and the magnitude of error. In fact, all the Pearson correlation coefficients for this test were below 0.2 (Figure 8).

Figure 9 shows the relationship between the standard deviation of error and the correlation between the external bellows signal and the ground-truth internal 6DoF motion. In the tested dataset, we found that there was a strong correlation between the external signal and the internal motion in the SI direction, as evident by the clustered values of the correlation values closer to 1 than the motion in any other degree of freedom.

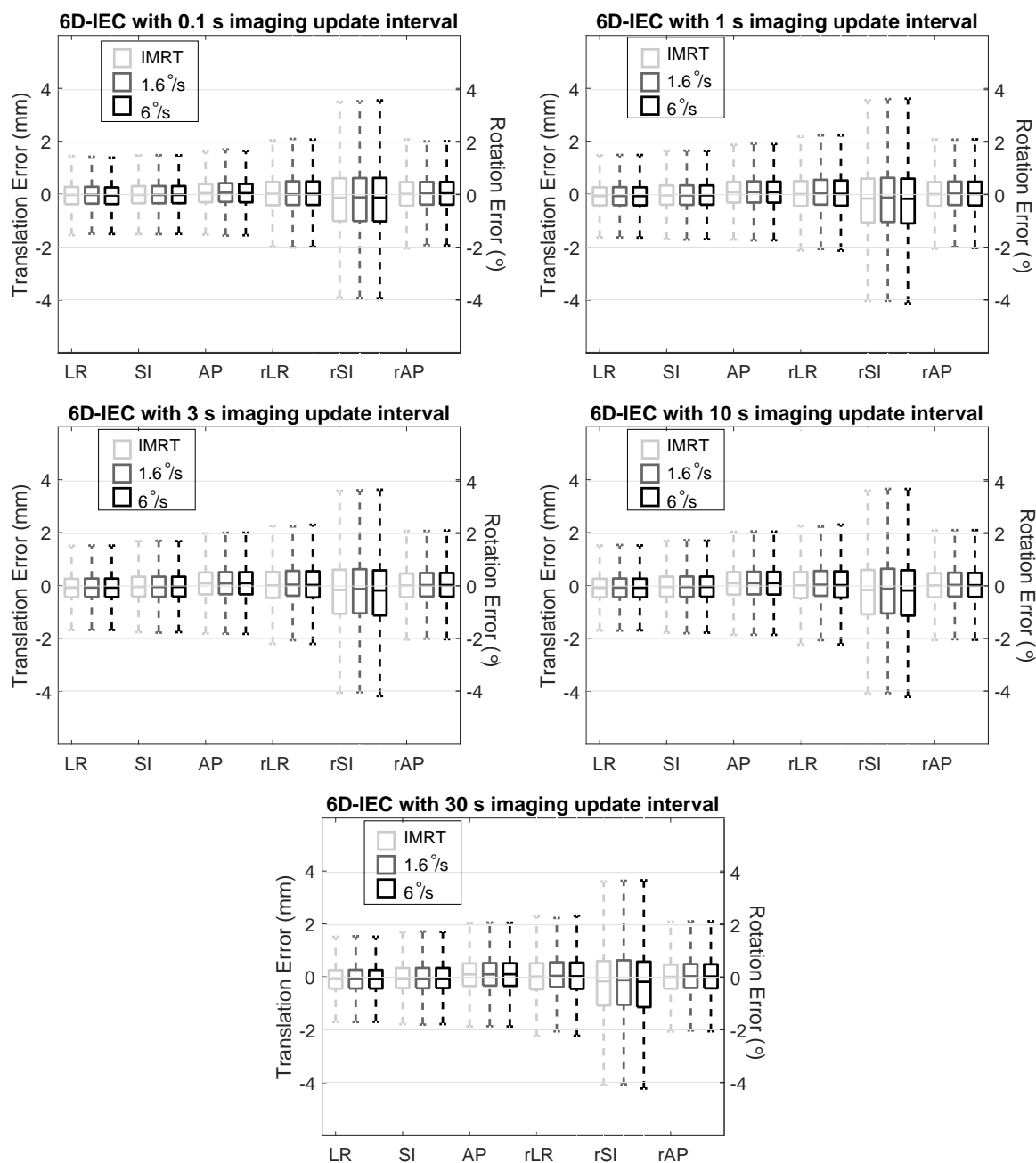


Figure 2. Boxplots of the error of 6D-IEC in estimating 6DoF lung tumour motion compared to the ground-truth motion for all tested scenarios. The tested dataset contain more than 17 hours recording of lung tumour motion from 6 lung cancer patients treated in both prone and supine postures in 19 fractions. The whiskers in each boxplot contain 99.9% of the data.

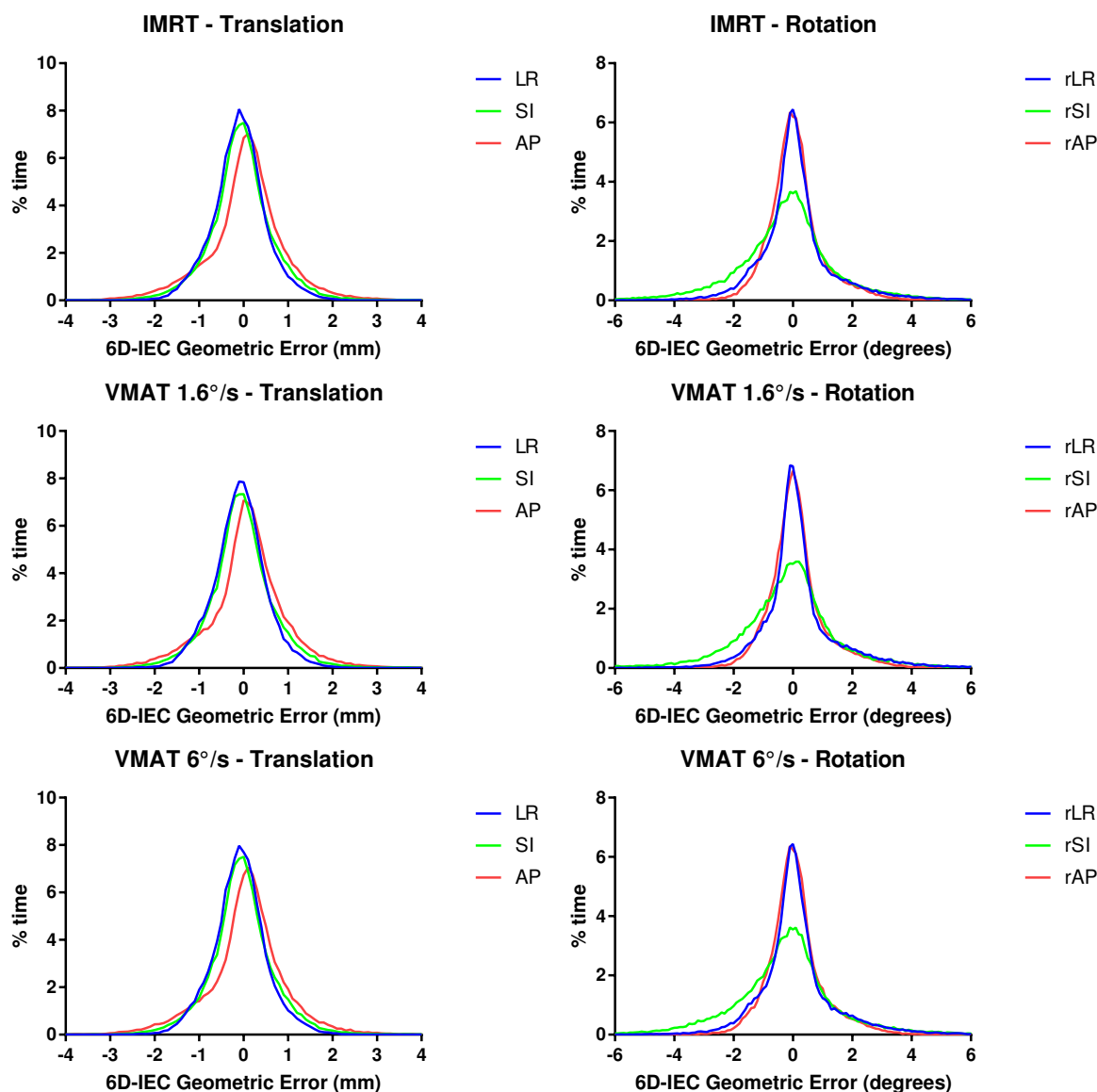


Figure 3. Relative frequency distributions (as percentages of time) of geometric errors for all the tested clinical scenario with imaging update interval of 30 s.

Furthermore, there was a strong negative correlation between the standard deviation of error and the internal-external correlation value for the motion in the SI direction ($\rho = -0.7$). This strong negative correlation was not found for the motion in any other degrees of freedom for the motion. We also found a strong positive correlation between the standard deviation or error and the internal-external correlation for rotational motion around the SI axis (rSI). Notably, rotational motion round the SI axis had the lowest internal-external correlation among all the six degrees of freedom, with most of the values less than 0.5.

In Figure 10, the relationship between the optimal phase augmentation parameter

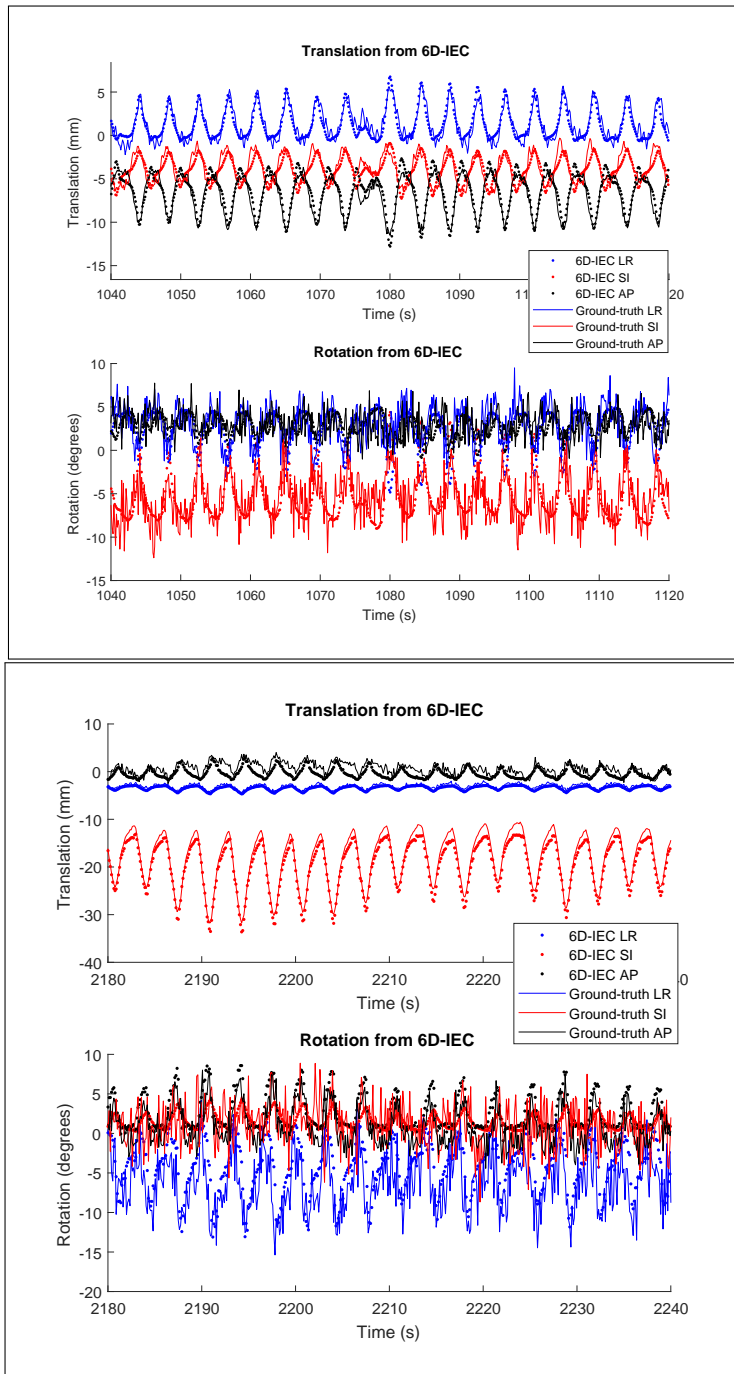


Figure 4. Two examples where the 6D-IEC algorithm was successful in estimating 6DoF tumour motion with one projection every 30 seconds during a slow gantry rotation VMAT treatment ($1.6^\circ/s$) after an initial learning arc of 60 seconds. **Top** (Patient 5, fraction 4): an example where 6D-IEC was successful in estimating tumour motion with large rotations ($\sim 15^\circ$ peak-to-peak in rSI), and with large translational AP (~ 10 mm) and LR (~ 5 mm) motion compared to SI motion. The errors in this case were: LR: 0.2 ± 0.9 mm, SI: -0.1 ± 0.9 mm, AP: 0.2 ± 0.9 mm, rLR: $-0.3 \pm 1.9^\circ$, rSI: $0.3 \pm 2.3^\circ$ and rAP: $-0.3 \pm 1.4^\circ$. **Bottom** (Patient 6, Fraction 1): an example where 6D-IEC was successful in estimating tumour internal 6DoF motion for the fraction with the largest intrafraction motion (~ 20 mm in SI) in this dataset. The errors in this case were: LR: 0.3 ± 0.3 mm, SI: -0.7 ± 0.9 mm, AP: -0.5 ± 1.0 mm, rLR: $2.3 \pm 2.5^\circ$, rSI: $0.48 \pm 2.04^\circ$ and rAP: $1.38 \pm 1.37^\circ$.

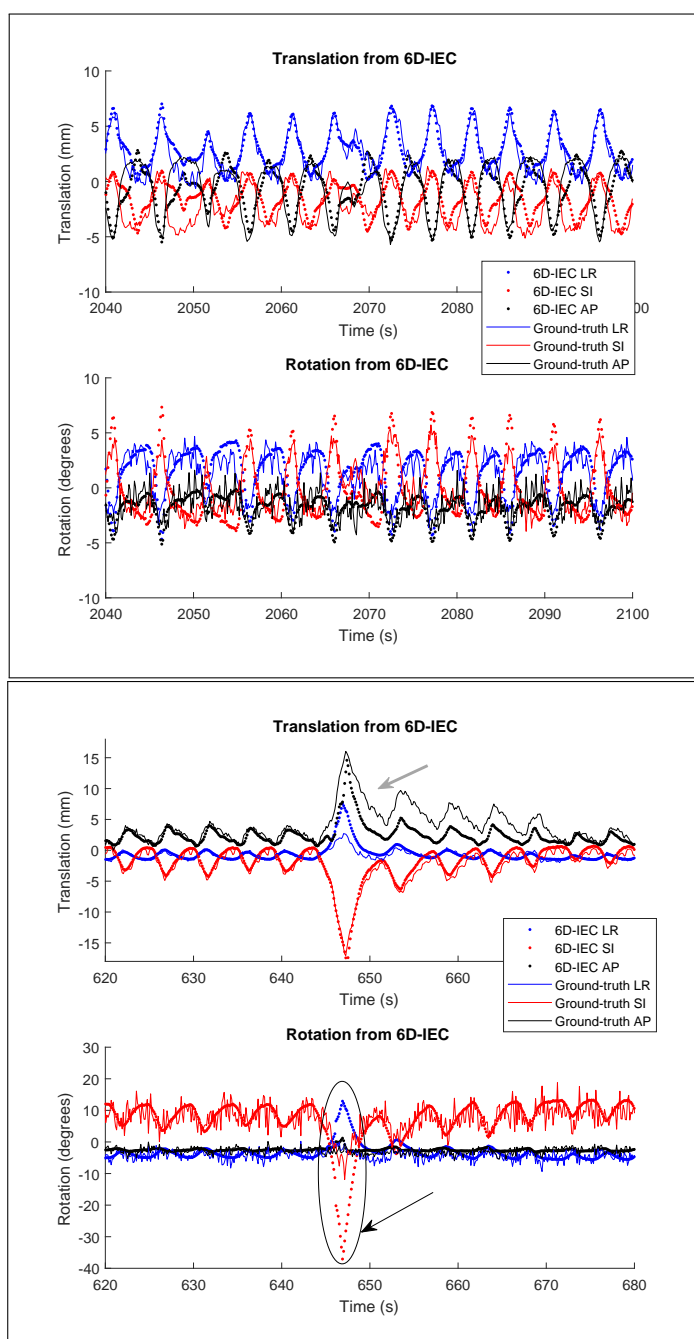


Figure 5. Two challenging examples for the 6D-IEC algorithm in the tested dataset. Motion tracking are shown with one projection every 30 seconds during a slow gantry rotation VMAT treatment ($1.6^\circ/s$) after an initial learning arc of 60 seconds. **Top:** an example (Patient 5, fraction 2) where 6D-IEC was successful in estimating translations but over-estimated rotational motion; the errors were: LR: 0.1 ± 1.0 mm, SI: 0.4 ± 1.3 mm, AP: 0.2 ± 1.2 mm, rLR: $0.6 \pm 1.6^\circ$, rSI: $-0.3 \pm 1.6^\circ$ and rAP: $-0.1 \pm 0.8^\circ$. **Bottom:** an example (Patient 4, fraction 0) where 6D-IEC struggled due to the sudden change in correlation, leading to over-estimation of rotation during a cough (black arrow) followed by under-estimation of translation in the AP direction after the cough (grey arrow). In this case, the errors were LR: 0.0 ± 0.3 mm, SI: -0.1 ± 0.5 mm, AP: -1.0 ± 1.0 mm, rLR: $0.6 \pm 1.4^\circ$, rSI: $0.6 \pm 2.7^\circ$, and rAP: $0.4 \pm 0.7^\circ$.

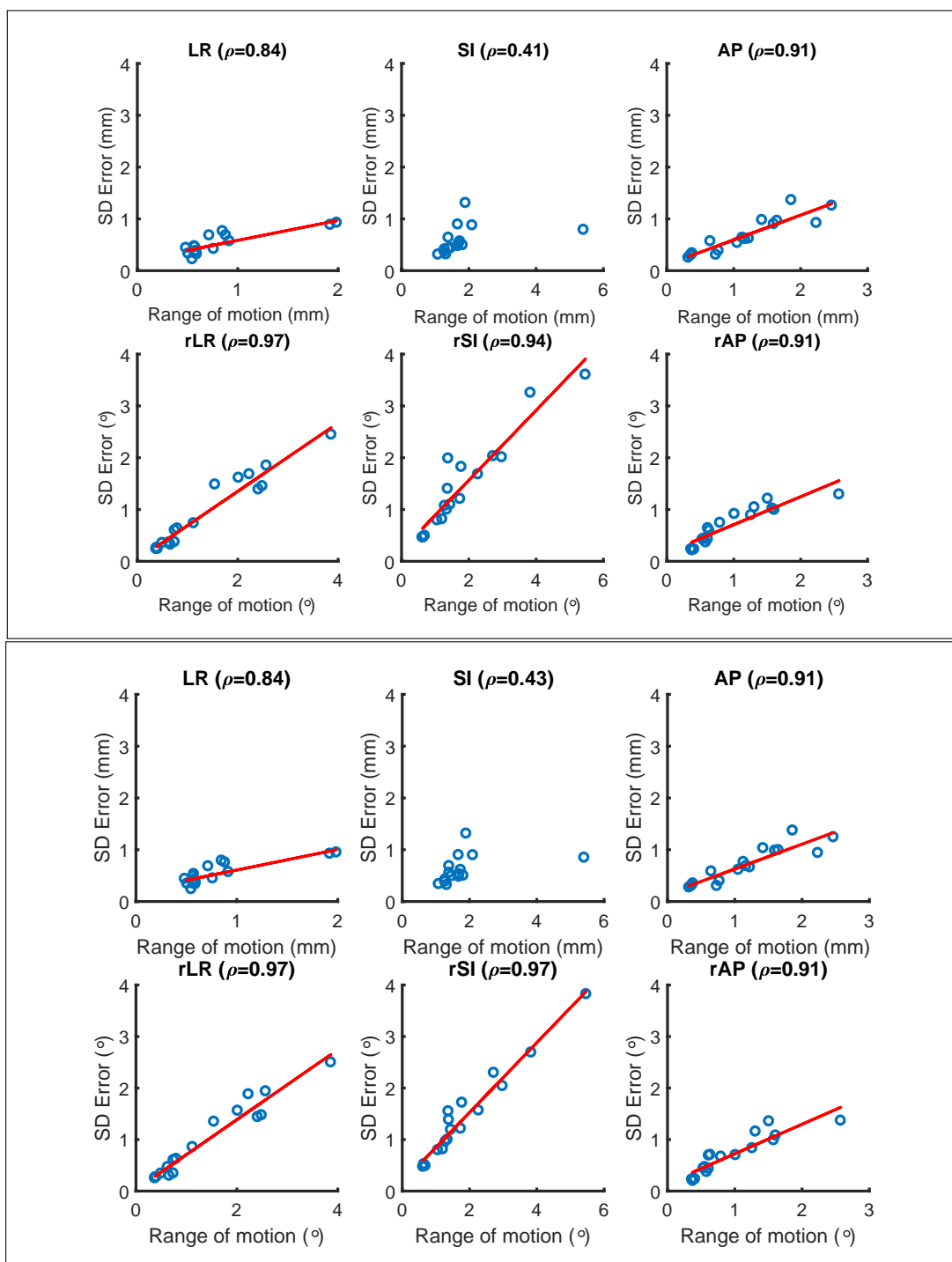


Figure 6. Scatter plots of the effect of the range of motion on 6D-IEC precision, measured as the standard deviation of the difference between 6D-IEC estimates and the ground-truth motion. **Top:** With the largest standard deviation of error (VMAT $1.6^\circ/s$) at the highest interval between imaging update (30 s). **Bottom:** With the lowest standard deviation of error (VMAT $6^\circ/s$) at the most frequent imaging update (0.1 s).

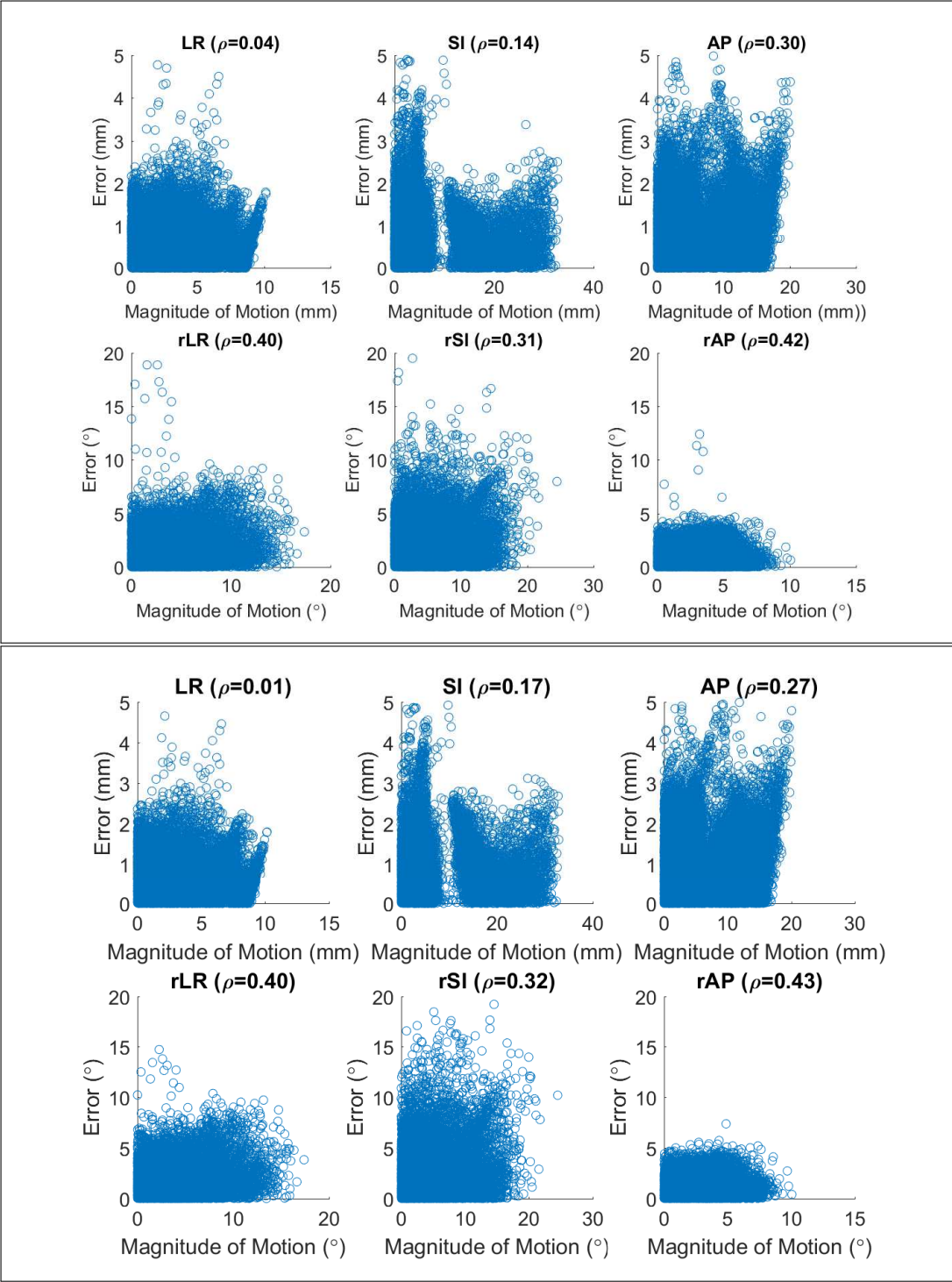


Figure 7. Scatter plots of the effect of the magnitude of motion on 6D-IEC performance, measured as the the difference between 6D-IEC estimates and the ground-truth motion. **Top:** With the largest standard deviation of error (VMAT 1.6°/s) at the highest interval between imaging update (30 s). **Bottom:** With the lowest standard deviation of error (VMAT 6°/s) at the most frequent imaging update (0.1 s).

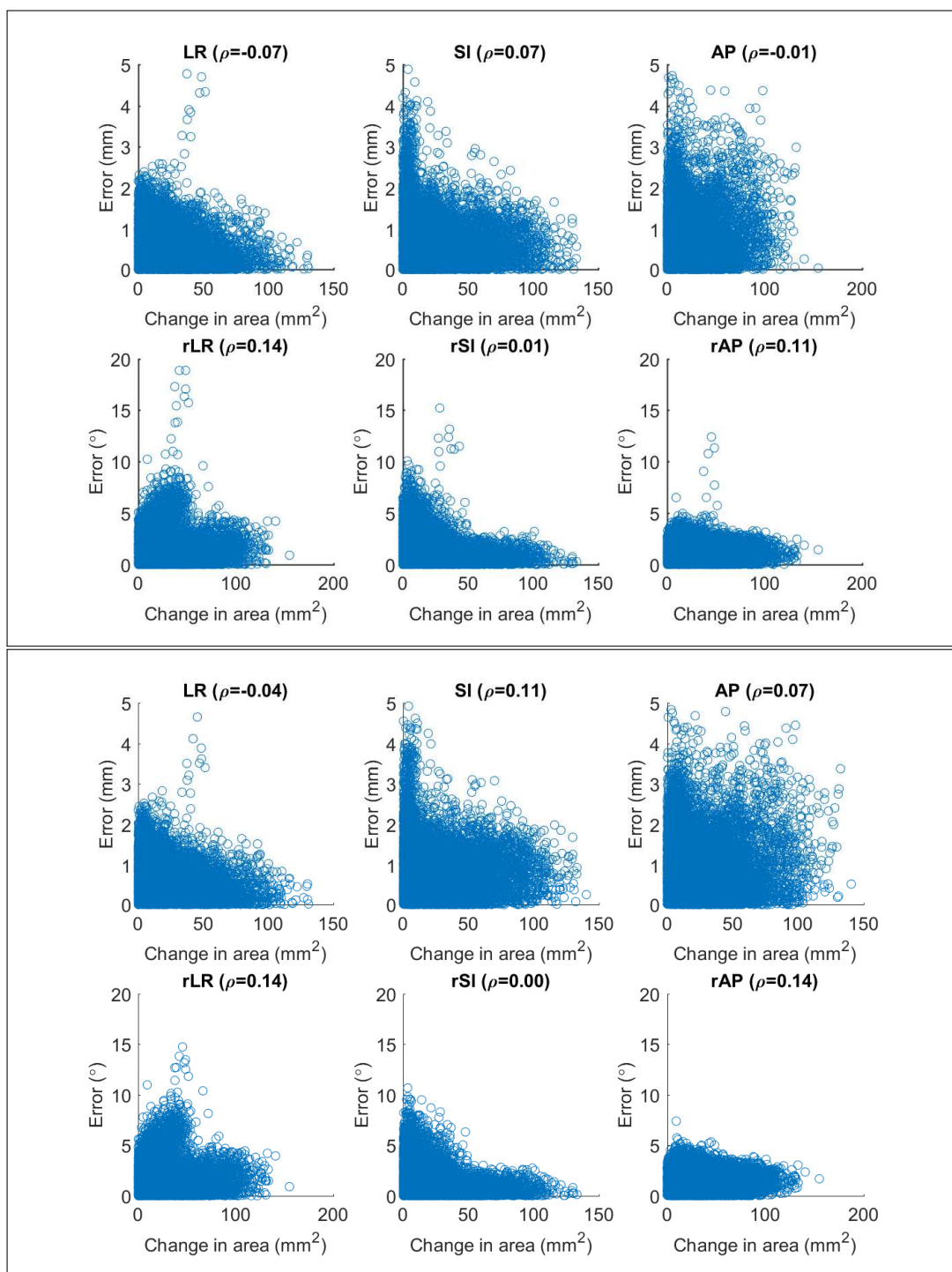


Figure 8. Scatter plots of the effect of deformation on 6D-IEC performance, measured as the the difference between 6D-IEC estimates and the ground-truth motion. Deformation was measured as the change in the area of the 3D triangle formed by the 3 Calypso beacons during the tracking phase compared to their initial positions. **Top:** With the largest standard deviation of error (VMAT 1.6°/s) at the highest interval between imaging update (30 s). **Bottom:** With the lowest standard deviation of error (VMAT 6°/s) at the most frequent imaging update (0.1 s).

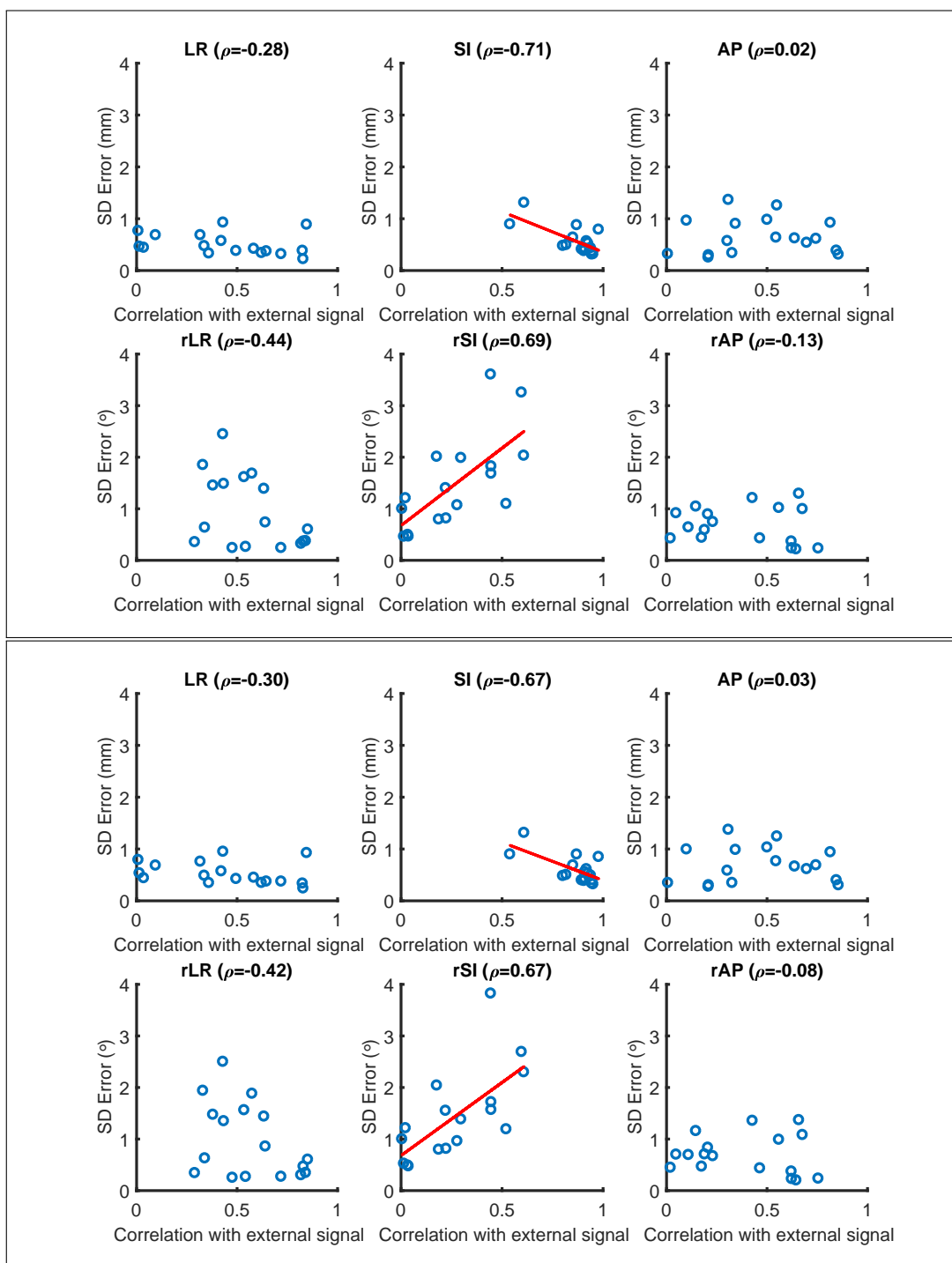


Figure 9. Scatter plots of the effect of the external-internal correlation on 6D-IEC precision, measured as the standard deviation of the difference between 6D-IEC estimates and the ground-truth motion. **Top:** With the largest standard deviation of error (VMAT 1.6°/s) at the highest interval between imaging update (30 s). **Bottom:** With the lowest standard deviation of error (VMAT 6°/s) at the most frequent imaging update (0.1 s).

(λ) and the standard deviation of 6D-IEC error in estimating the motion in each degree of freedom is depicted. As shown in Figure 10, an increase in the (λ) value correlated with an increase in standard deviation of errors in the translational LR motion ($\rho = 0.7$) and SI motion ($\rho = 0.6$) while having no discernible effect on motion in any other degrees of freedom.

4. Discussion

We developed and evaluated a novel method for highly accurate real-time 6DoF motion monitoring by combining continuous external signal and intermittent imaging, thus enabling real-time 6DoF motion monitoring for patients on a standard linac without requiring continuous high frequency kV imaging. The developed 6D-IEC method leverages external respiratory signal, which has high temporal resolution (40Hz) for continuous real-time estimation of 6DoF tumour motion during treatment. In our approach, a 6DoF internal-external correlation model (6D-IEC), which has a state-augmentation parameter to account for possible hysteresis, was optimised using a least-square optimisation method. The 6D-IEC correlation model uses frequent 2D imaging during pre-treatment CBCT and the continuous external signal to solve for its parameters without requiring an intermediate 3D estimation step. This system then uses intermittent kV images to re-optimize the state augmented correlation model to account for baseline drifts during the duration of the treatments and changes to the correlations.

In order to evaluate the framework, we obtained 2D positions of the 3 implanted transponders by projecting the 3D positions onto a typical kV X-ray imaging system of a typical linear accelerator. The work thus assumed that at least 3 unique 2D positions representing the tumour can be obtained on the acquired 2D images during both CBCT to initiate the model and during treatment for updating it. In fact, three is the lowest number of 2D positions that would allow a unique solution for the correlation coefficients to be found for all six degrees of freedom. In a clinical scenario, these points would come from the segmentation of the tumours or of implanted radio-opaque markers that act as surrogates for the tumour on a kV image. The presented results also assume perfect segmentation of the markers' positions.

The accuracy and precision of 6D-IEC in estimating 6DoF tumour motion during treatment was evaluated using a ground-truth dataset of 6 patients with implanted electromagnetic transponders for lung SABR treatments. Three different clinical treatment scenarios were simulated to test the accuracy of 6D-IEC, including: 5 field IMRT treatment with a 40 s delivery time for each field, slow gantry speed VMAT treatment at $1.6^\circ/s$ and fast gantry speed VMAT treatment at $6^\circ/s$. All simulated treatment scenarios start with a 60 s of pre-treatment CBCT. During the simulated treatment phase, for each treatment scenario, the 6D-IEC algorithm was evaluated for different imaging update intervals during the tracking period, including: 0.1 s, 1 s, 3 s, 10 s and 30 s. Overall, in each of the imaging update intervals during the tracking phase,

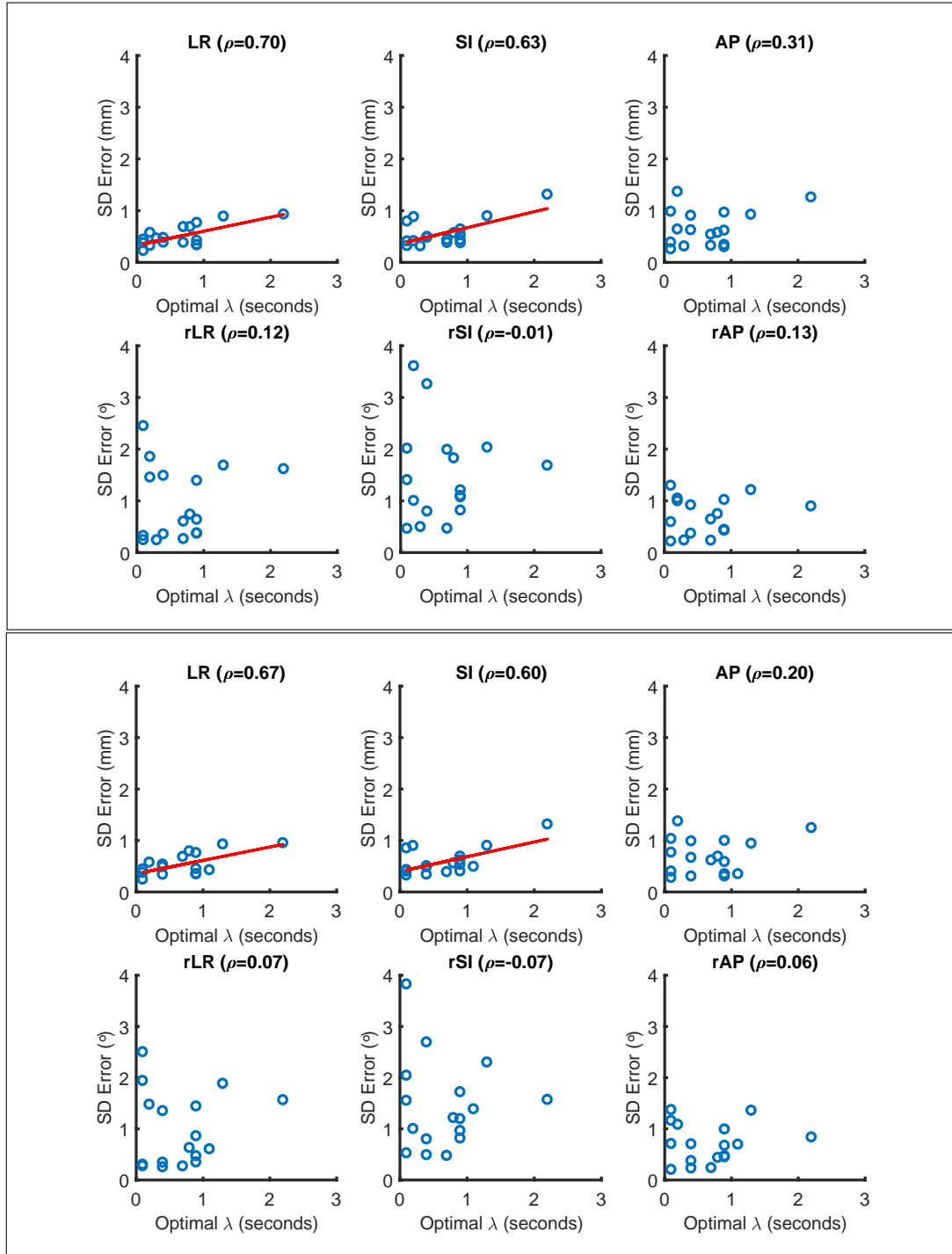


Figure 10. Scatter plots of the relationship between the phase augmentation parameter λ and 6D-IEC precision, measured as the standard deviation of the difference between 6D-IEC estimates and the ground-truth motion. **Top:** With the largest standard deviation of error (VMAT 1.6°/s) at the highest interval between imaging update (30 s). **Bottom:** With the lowest standard deviation of error (VMAT 6°/s) at the most frequent imaging update (0.1 s).

the errors in all 6DoFs were similar for both IMRT and VMAT treatment scenarios (gantry speed of $1.6^\circ/s$ and $6^\circ/s$) with sub-mm translational accuracy and precision and sub-degree accuracy for rotational motion with a precision of 2° . The accuracy and precision of 6D-IEC is thus comparable with previous works in estimation of real-time 6DoF motion using continuous kV imaging (Kim et al. 2017). An additional strength of this work is that our method was evaluated using *true* internal motion from implanted electromagnetic transponders, thus, removing any bias of the result due to using data where internal-external correlation was assumed (Montanaro et al. 2018).

The reported accuracy and precision of 6D-IEC in the *in silico* evaluation assumed perfect segmentation of the markers in each incoming projection image. Compared to systems such as KIM which relies heavily on accurate marker segmentation, 6D-IEC would be more tolerant to marker segmentation error as the correlation model can be selectively rebuilt when the segmentation returns highly confident results. Further experimental studies are required to investigate the accuracy and precision of 6D-IEC in realistic clinical scenarios with anthropomorphic phantoms.

In all tested scenarios, the standard deviation of translational and rotational errors increased slightly as the imaging update interval increases (Table 1 and Figure 2). This result agrees with previous studies in estimating 3D tumour motion based on external signal surrogacy (Cho et al. 2010, Hoogeman et al. 2009), both of which showed an increase in imaging update interval causes only small increases in motion estimation error. Cho et al. (2010) found that as the imaging interval increased from 10 s to 200 s, the 3D root-mean-square error of their motion estimation increased only by 0.2 mm. We found with our method, on the evaluated dataset, that increasing the imaging interval from 100 ms to 30 s only increased the standard deviation of error by a maximum of 0.1 mm for translational motion and 0.1° for rotational motion. These results suggest that the correlation between the internal tumour motion and the external surrogate signal is stable over a long period of time for most patients. However, these results are averaged values of a large database of many fractions. In reality, sudden changes to the external-internal correlation can occur due to changes in a patient’s physiology during treatment, e.g. Figure 5.

Among the factors that could influence the accuracy and precision of the presented 6D-IEC method, the range of motion in each fraction had a strong effect. The relationship is universally strongly positively correlated: the higher the motion range, the larger the estimation error. The implication is that, fundamentally, even including the phase augmentation parameter, the complex relationship between internal tumour motion and the external motion cannot be fully encapsulated with a linear equation (e.g. Equation 1). In addition, we only use a one-dimensional signal to approximate 6DoF internal motion. The approximation gradually breaks down as the motion magnitude becomes larger and more complex. Furthermore, the error of the method also increases when the linear correlation between the external signal and the internal motion in each of the 6DoF decreases, as shown in Figure 9. In the present work, the largest error was found in estimating the rotational motion around the SI axis, which also has the lowest

linear correlation with the external signal.

It was also found that the value of the phase shift parameter has an effect on the error in estimating translational motion in the LR and SI direction, and to a lesser extent translational motion in the AP direction. A larger phase shift indicates more hysteresis between the internal motion and the external surrogate, i.e., how far out of phase one signal is from the other. As hysteresis increases, the linear approximation also gradually becomes less accurate. Although Ruan et al. (2008) and Cho et al. (2010) both found that a fixed value of phase shift up around 1 s is adequate on their tested data, in the development of the 6D-IEC method, we found that a phase selection to iteratively determine the optimal value of the phase augmentation parameter makes the model more stable.

5. Conclusion

The present work describes, to the best of our knowledge, the first method to estimate real-time tumour 6DoF motion without using continuous kV imaging. Our 6D-IEC method can thus enable real-time high temporal resolution monitoring for 6DoF tumour motion on any standard linear accelerators with optical (e.g. Varian RPM or OSMS) or mechanical respiratory sensors (bellows belt or spirometry) whilst exposing the patient to $\leq 1\%$ of the imaging dose (intrafraction kV imaging every 10 s or 30 s instead of every 0.1 s). Assuming perfect target segmentation on kV images, the presented system has sub-mm and sub-degree accuracy for lung tumour motion monitoring. As kV images are only needed occasionally for 6D-IEC, this method can be broadly applicable for both co-planar and non-coplanar treatments, providing highly accurate tumour 6DoF motion monitoring for precise radiotherapy treatments.

Acknowledgment

The authors thank Dr Helen Ball for her proofreading and valuable inputs in improving the clarity of this manuscript. This work is funded by an NHMRC grant (APP1138807). Author D T Nguyen is funded by an NHMRC Early Career Research Fellowship and a Cancer Institute New South Wales Early Career Fellowship. Author P J Keall acknowledges funding from an NHMRC Senior Principal Research Fellowship.

References

- Amro, H., Hamstra, D. A., Mcshan, D. L., Sandler, H., Vineberg, K., Hadley, S. & Litzenberg, D. (2013), 'The dosimetric impact of prostate rotations during electromagnetically guided external-beam radiation therapy', *Int J Radiat Oncol Biol Phys* **85**(1), 230–236.
- Aubry, J.-F., Beaulieu, L., Girouard, L.-M., Aubin, S., Tremblay, D., Laverdure, J. & Vigneault, E. (2003), 'Measurements of intrafraction motion and interfraction and

- intrafraction rotation of prostate by three-dimensional analysis of daily portal imaging with radiopaque markers', *Int J Radiat Oncol Biol Phys* **60**(1), 30–39.
- Ballhausen, H., Li, M., Hegemann, N.-S., Ganswindt, U. & Belka, C. (2015), 'Intrafraction motion of the prostate is a random walk', *Phys Med Biol* **60**(2).
- Bertholet, J., Toftegaard, J., Hansen, R., Worm, E. S., Wan, H., Parikh, P. J., Weber, B., Hoyer, M. & Poulsen, P. R. (2018), 'Automatic online and real-time tumour motion monitoring during stereotactic liver treatments on a conventional linac by combined optical and sparse monoscopic imaging with kilovoltage x-rays (cosmik)', *Phys. Med. Biol.* .
- Bertholet, J., Worm, E. S., Fledelius, W., Hyer, M. & Poulsen, P. R. (2016), 'Time-resolved intrafraction target translations and rotations during stereotactic liver radiation therapy: Implications for marker-based localization accuracy.', *Int J Radiat Oncol Biol Phys* **95**(2), 802–809.
- Booth, J. T., Caillet, V., Hardcastle, N., O'Brien, R., Szymura, K., Crasta, C., Harris, B., Haddad, C., Eade, T. & Keall, P. (2016), 'The first patient treatment of electromagnetic-guided real time adaptive radiotherapy using mlc tracking for lung sabr', *Radiother Oncol* **121**(1), 19–25.
- Castellanos, E., Ericsson, M. H., Sorcini, B., Green, U., Nilsson, S. & Lennerns, B. (2012), 'Raypilot electromagnetic real-time positioning in radiotherapy of prostate cancer initial clinical results', *Radiother Oncol* **103**(suppl 1), S433.
- Cho, B., Poulsen, P. R. & Keall, P. J. (2010), 'Real-time tumor tracking using sequential kv imaging combined with respiratory monitoring: a general framework applicable to commonly used igrt systems.', *Phys. Med. Biol.* **55**, 32993316.
- Cho, B., Poulsen, P. R., Ruan, D., Sawant, A. & Keall, P. J. (2012), 'Experimental investigation of a general real-time 3d target localization method using sequential kv imaging combined with respiratory monitoring', *Phys Med Biol* **57**, 7395–7407.
- Chung, H., Poulsen, P. R., Keall, P. J., Cho, S. & Cho, B. (2016), 'Reconstruction of implanted marker trajectories from cone-beam ct projection images using interdimensional correlation modeling', *Med Phys* **43**(8), 4643–4654.
- Fallone, B. G., Murray, B., Rathee, S., Stanescu, T., Steciw, S., Vidakovic, S., Blosser, E. & Tymofichuk, D. (2009), 'First mr images obtained during megavoltage photon irradiation from a prototype integrated linac-mr system', *Med Phys* **36**, 2084–2088.
- Hoogeman, M., Prevost, J. B., Nuyttens, J., Poll, J., Levendag, P. & Heijmen, B. (2009), 'Clinical accuracy of the respiratory tumor tracking system of the cyberknife: assessment by analysis of log files', *Int. J. Radiat. Oncol. Biol. Phys.* **74**, 297303.
- Huang, C.-Y., Tehrani, J. N., Ng, J. A., Booth, J. T. & Keall, P. J. (2015), 'Six degrees-of-freedom prostate and lung tumor motion measurements using kilovoltage intrafraction monitoring', *Int J Radiat Oncol Biol Phys* **91**(2), 368–375.
- Kim, J., Nguyen, D., Huang, C., Fuangrod, T., Caillet, V., O'Brien, R., Poulsen, P., Booth, J. & Keall, P. (2017), 'Quantifying the accuracy and precision of a novel real-

- time 6 degree-of-freedom kilovoltage intrafraction monitoring (kim) target tracking system', *Physics in medicine and biology* **62**(14), 5744–5759.
- Kitamura, K., Shirato, H., Seppenwoolde, Y., Onimaru, R., Oda, M., Fujita, K., Shimizu, S., Shinohara, N., Harabayashi, T. & Miyasaka, K. (2002), 'Three-dimensional intrafractional movement of prostate measured during real-time tumor-tracking radiotherapy in supine and prone treatment positions', *Int J Radiat Oncol Biol Phys* **53**(5), 1117–11123.
- Kupelian, P., Willoughby, T., Mahadevan, A., Djemil, T., Weinstein, G., Jani, S., Enke, C., Solberg, T., Flores, N., Liu, D., Beyer, D. & Levine, L. (2007), 'Multi-institutional clinical experience with the calypso system in localization and continuous, real-time monitoring of the prostate gland during external radiotherapy', *Int J Radiat Oncol Biol Phys* **67**(4), 1088–1098.
- Li, R., Fahimian, B. P. & Xing, L. (2011), 'A bayesian approach to real-time 3d tumor localization via monoscopic x-ray imaging during treatment delivery', *Med Phys* **38**, 4205–4214.
- Montanaro, T., Nguyen, D. T., Keall, P. J., Booth, J., Caillet, V., Eade, T., Haddad, C. & Shieh, C. C. (2018), 'A comparison of gantry-mounted x-ray based real-time target tracking methods', *Med. Phys.* **45**, 1222–1232.
- Nguyen, D. T., Kim, J.-H., O'Brien, R. T., Huang, C.-Y., Booth, J. T., Greer, P., Legge, K., Poulsen, P. R., Martin, J. & Keall, P. J. (2017), 'The first clinical implementation of a real-time six degree of freedom tracking system during radiation therapy', *Radiother Oncol* [**In Press**].
- Poulsen, P. R., Cho, B., Langen, K., Kupelian, P. & Keall, P. J. (2008), 'Three-dimensional prostate position estimation with a single x-ray imager utilizing the spatial probability density', *Phys Med Biol* **53**(16), 4331–4353.
- Raaymakers, B. W., Lagendijk, J. J. W., Overweg, J., Kok, J. G. M., Raaijmakers, A. J. E., Kerkhof, E. M., Put, R. W. v. d., Meijnsing, I., Crijns, S. P. M. & Benedosso, F. (2009), 'Integrating a 1.5 t mri scanner with a 6 mv accelerator: proof of concept', *Phys Med Biol* **54**, N229.
- Rijkhorst, E.-J., Lakeman, A., Nijkamp, J., Bois, J. d., Herk, M. v., Lebesque, J. V. & Sonke, J.-J. (2009), 'Strategies for online organ motion correction for intensity-modulated radiotherapy of prostate cancer: Prostate, rectum, and bladder dose effects', *Int J Radiat Oncol Biol Phys* **75**(4), 1254–1260.
- Ruan, D., Fessler, J. A., Balter, J. M., Berbeco, R. I., Nishioka, S. & Shirato, H. (2008), 'Inference of hysteretic respiratory tumor motion from external surrogates: A state augmentation approach', *Phys Med Biol* **53**, 2923–2936.
- Sazawa, A., Shinohara, N., Harabayashi, T., Abe, T., Shirato, H. & Nonomura, K. (2009), 'Alternative approach in the treatment of adrenal metastasis with a real-time tracking radiotherapy in patients with hormone refractory prostate cancer.', *Int J Urol.* **16**(4), 410–412.

- Shieh, C., Caillet, V., Dunbar, M., Keall, P., Booth, J., Hardcastle, N., Haddad, C. and Eade, T. & Feain, I. (2017), ‘A bayesian approach for three-dimensional markerless tumor tracking using kv imaging during lung radiotherapy.’, *Physics in Medicine and Biology* **62**, 3065–3080.
- Shirato, H., Harada, T., Harabayashi, T., Hida, K., Endo, H., Kitamura, K., Onimaru, R., Yamazaki, K., Kurauchi, N., Shimizu, T., Shinohara, N., Matsushita, M., Dosaka-Akita, H. & Miyasaka, K. (2003), ‘Feasibility of insertion/implantation of 2.0-mm-diameter gold internal fiducial markers for precise setup and real-time tumor tracking in radiotherapy.’, *Int J Radiat Oncol Biol Phys* **56**(1), 240–247.
- Stevens, M. T., Parsons, D. D. & Robar, J. L. (2016), ‘Continuous monitoring of prostate position using stereoscopic and monoscopic kv image guidance’, *Medical Physics* **43**, 2558–2568.
- Tehrani, J. N., O’Brien, R. T., Poulsen, P. R. & Keall, P. (2013), ‘Real-time estimation of prostate tumor rotation and translation with a kv imaging system based on an iterative closest point algorithm’, *Phys Med Biol* **58**(23), 8517–8533.
- Wu, J., Ruan, D., Cho, B., Sawant, A., Petersen, J., Newell, L. J., Cattell, H. & Keall, P. J. (2011), ‘Electromagnetic detection and real-time dmlc adaptation to target rotation during radiotherapy’, *Int J Radiat Oncol Biol Phys* **82**(3), e545–e553.